

Article

Construction of High-Activity Nano-NiTiO₃/g-C₃N₄ Composite Catalysts for Enhanced Photodegradation Activities under Visible Light

Da Li ¹, Zhan Yang ¹, Kun Wang ², Lan Zhang ², Linglong Shi ¹, Abdul Qadeer ², Jiao Dong ^{2,*} and Haoyu Ren ^{2,*}

¹ School of Environmental Science and Engineering, Qilu University of Technology, Shandong Academy of Sciences, Jinan 250353, China; lidashenxian@126.com (D.L.); yangzhan531@163.com (Z.Y.); sll18788514153@126.com (L.S.)

² National Engineering Laboratory for Lake Pollution Control and Ecological Restoration, State Environment Protection Key Laboratory for Lake Pollution Control, Chinese Research Academy of Environmental Sciences, Beijing 100012, China; wangkun_1015@126.com (K.W.); zhanglan3524@163.com (L.Z.); dr.aq.geographer@gmail.com (A.Q.)

* Correspondence: dongjiao_1989@163.com (J.D.); rhy@mail.bnu.edu.cn (H.R.)

Abstract: Nickel titanate (NiTiO₃) semiconductors and graphitic carbon nitride (g-C₃N₄) have attracted great attention as photocatalysts in the degradation of environmental pollutants because of their visible-light-driven activity. But the utilizations of both semiconductors are limited by their low specific surface area. In this study, a nano-NiTiO₃/g-C₃N₄ photocatalyst was successfully synthesized by optimizing the preparation method of photocatalyst precursors. Compared with the bulk g-C₃N₄ and bulk NiTiO₃/g-C₃N₄ composite photocatalysts, the nano-NiTiO₃/g-C₃N₄ composite catalyst displayed a larger specific surface area, a more abundant pore size structure, and superior carrier separation capabilities. According to the pseudo-first-order, the degradation rate of MB was more than 2.5–19.7 times higher than that of previous studies. The superoxide radicals ($\cdot\text{O}_2^-$) and holes (h^+) played significant roles in the photocatalytic reaction of MB. This study provides a new idea for the synthesis of photocatalysts and the improvement in photocatalytic performance.

Keywords: nano-NiTiO₃/g-C₃N₄; photodegradation; visible light; high activity; photodegradation mechanism



Citation: Li, D.; Yang, Z.; Wang, K.; Zhang, L.; Shi, L.; Qadeer, A.; Dong, J.; Ren, H. Construction of High-Activity Nano-NiTiO₃/g-C₃N₄ Composite Catalysts for Enhanced Photodegradation Activities under Visible Light. *Separations* **2024**, *11*, 77. <https://doi.org/10.3390/separations11030077>

Academic Editor: Dimosthenis Giokas

Received: 8 January 2024

Revised: 14 February 2024

Accepted: 24 February 2024

Published: 1 March 2024



Copyright: © 2024 by the authors. Licensee MDPI, Basel, Switzerland. This article is an open access article distributed under the terms and conditions of the Creative Commons Attribution (CC BY) license (<https://creativecommons.org/licenses/by/4.0/>).

1. Introduction

One of the biggest challenges of the 21st century is environmental pollution caused by refractory organic matter, demanding the development of efficient and environmentally friendly technologies as a solution [1]. Among these, photocatalytic technology has gained recognition for its effectiveness in degrading pollutants. Studies have demonstrated that when exposed to sunlight, photocatalysts can undergo excitation, leading to the generation of photoelectrons, vacancies, and free radicals, all of which contribute to pollutant degradation [2]. The discovery by Wang et al. that graphite carbon nitride (g-C₃N₄) can be hydrolyzed to produce hydrogen has sparked significant interest in this material due to its metal-free nature, exceptional thermal and chemical stability, and suitable band gap [3,4]. However, bulk g-C₃N₄ possesses certain drawbacks, such as a high rate of recombination of electron-hole pairs and a limited specific surface area, which hinder its photocatalytic efficiency [5]. To address these challenges, two effective approaches have been proposed. Firstly, the preparation of g-C₃N₄ nanosheets offers a viable solution, enhancing the specific surface area and adsorption capacity. Secondly, the formation of heterojunctions with semiconductors presents another avenue for improvement, expanding the materials' responsiveness to visible light and mitigating the recombination rate of photoelectrons and holes [6,7].

The unique physical and chemical properties of g-C₃N₄ nanostructures have been documented, offering potential solutions to address challenges related to electron–hole pair recombination and low specific surface area resulting from the π - π conjugation system [8]. Xu et al. achieved successful preparation of g-C₃N₄ nanostructures by introducing bulk g-C₃N₄ to concentrated sulfuric acid and stirring the mixture for 8 h [9]. In a separate study, Yang et al. employed ball milling and liquid exfoliation techniques to produce nanostructured g-C₃N₄, which exhibited a high degradation rate for RhB [10]. Another approach involved the utilization of mesoporous silica as a template and monocyanidamide as a precursor in the study by Groenewolt et al., who constructed porous g-C₃N₄ nanostructures through thermal polymerization with an HF solution etching method. The resulting g-C₃N₄ nanosheets displayed a larger specific surface area compared to direct thermal polymerization [11]. However, the liquid exfoliation method suffered from a low yield and a complicated preparation procedure, while the template method employed a significant quantity of chemical auxiliary reagents, increasing the risk of environmental pollution. Alternatively, the hydrothermal synthetic method has been reported as an efficient means of preparing g-C₃N₄ nanostructures [12]. It has been demonstrated that g-C₃N₄ nanostructures synthesized through hydrothermal methods exhibit improved photocatalytic water-splitting performance [13]. Nonetheless, the band gap of g-C₃N₄ nanostructures synthesized via the hydrothermal method tends to be wide, resulting in low light-energy efficiency.

In recent years, extensive research has been conducted to address the issue of low light-energy efficiency in g-C₃N₄, resulting in the investigation of numerous heterojunctions based on g-C₃N₄. Notably, a study by Jung et al. (2018) discovered that ZnO/g-C₃N₄ heterojunctions effectively enhance the separation of electron–hole pairs and enhance photocatalytic activity [14]. Similarly, Gu et al. (2015) observed that TiO₂/g-C₃N₄ heterojunctions, which were synthesized, exhibited commendable efficiency in the degradation of methylene blue and rhodamine B through photocatalysis [15]. Furthermore, Fu et al. (2013) successfully constructed g-C₃N₄/CdS heterojunctions using an in situ precipitation method, resulting in a photocatalytic degradation activity that was 20.5 times higher than that of pure g-C₃N₄ and 3.1 times higher than that of CdS, demonstrating promising cyclic stability [16]. In the realm of perovskite titanates, Qu et al. (2012) reported significant photocatalytic properties of these materials in terms of oxidizing toxic organic pollutants and generating hydrogen (H₂) [17]. Specifically, nickel titanate (NiTiO₃) with an energy band gap of 2.20 eV has garnered considerable attention due to its suitable band gap and distinctive light response under visible light, leading to extensive research endeavors [18,19]. In their study, Qu et al. (2013) successfully fabricated a NiTiO₃/CdS heterojunction and observed a remarkable enhancement in its oxidative degradation capability compared to pure CdS [20]. Furthermore, it has been demonstrated that pure g-C₃N₄, possessing a band gap ranging from 2.5 to 2.9 eV, can form a heterojunction with NiTiO₃ [21]. Wang et al. (2015) discovered that the photocatalytic activity of NiTiO₃/g-C₃N₄ increased significantly upon the elimination of nitrobenzene [22]. Similarly, Zeng et al. (2016) reported that NiTiO₃/g-C₃N₄ nanocomposites exhibited superior performance in the production of photocatalytic hydrogen [6]. However, it is worth noting that the aforementioned studies utilized g-C₃N₄ with a limited specific surface area for the formation of the heterojunction, which significantly impacts the adsorption capacity of the heterojunction and consequently reduces the photocatalytic efficiency. The specific surface areas of g-C₃N₄ and NiTiO₃ synthesized by different methods shown in Table 1 are small. To address this limitation, some investigations have focused on enhancing the specific surface area and catalytic activity of the heterojunction through the utilization of nanomaterials [23]. Some studies had found that hydrothermal methods could improve the specific surface area and photocatalytic performance of photocatalysts [13,24].

Table 1. Specific surface areas of g-C₃N₄ and NiTiO₃ synthesized by different methods.

Photocatalyst	Precursor	Synthesis Method	Specific Surface Area	Reference
g-C ₃ N ₄	melamine	Calcining method	11.5 m ² /g	[25]
	melamine	Calcining method	24.35 m ² /g	[26]
	dicyandiamidine	Calcining method	7.24 m ² /g	[27]
	melamine	Hydrothermal methods	28.2 m ² /g	[28]
NiTiO ₃	nickel acetate, tetra-n-butyltitanate	Facile ethylene glycol-mediated method	23.1 m ² /g	[17]
	nickel acetate, tetra-n-butyltitanate	Sol-gel method	11.4 m ² /g	[24]

The aim of this study was to synthesize nano g-C₃N₄ /NiTiO₃ photocatalysts with a large specific surface area and high catalytic activity by improving the synthesis method and to investigate the effect of nanostructures on the photocatalytic degradation of organic compounds. This investigation entailed the construction of nano-NiTiO₃/g-C₃N₄ and bulk NiTiO₃/g-C₃N₄ composites, which were employed to explore their respective photodegradation capabilities toward methylene blue (MB) when exposed to visible light. The photochemical and electrochemical properties of the synthesized materials were thoroughly examined, and the underlying mechanism behind the degradation of methylene blue was also considered.

2. Experimental Section

2.1. Materials and Reagents

Melamine (Machlin-Lab, 99.0%), ethylene glycol (Machlin-Lab, >99%), nickel acetate (Machlin-Lab, 99.0%), titanium butoxide (Machlin-Lab, 99.0%), methylene blue (MB) (Machlin-Lab, >98.0%), and methanol (Machlin-Lab, 99.5%) were used in this study. Ultrapure water was used as a solvent throughout the experimental procedures.

2.2. Synthesis of Nano-NiTiO₃

Nano-NiTiO₃ was synthesized by the optimized glycol medium route [17]: 2.49 g nickel acetate was completely dissolved in 60 mL ethylene glycol (EG), stirred for 3 h to form a green solution, and 3.2 mL tetrabutyl titanate was added to the green solution and stirred for 3 h to form a light blue precipitate. The light blue sediments were washed three times with ultrapure water and alcohol, centrifuged for 30 min, and dried at 60 °C in a vacuum drying oven. The dried products were calcined at 600 °C for 2 h in a Muffle furnace. The nano-NiTiO₃ product was named NT.

2.3. Synthesis of Nanostructures g-C₃N₄ and Bulk g-C₃N₄

Bulk g-C₃N₄ was synthesized by direct thermal polymerization [23]: 10.0 g melamine was loaded into a crucible with a cover and heated to 550 °C at a 2.5 °C/min heating rate and kept for 4 h. The light yellow g-C₃N₄ product was named BG.

g-C₃N₄ nanostructures were synthesized by optimized thermal polymerization of melamine treated by a hydrothermal process [27]: 12.0 g melamine was put into 150 mL ultrapure water and stirred well. Then, the white suspensions were poured into a 200 mL Teflon-lined stainless steel hydrothermal reactor and heated at 200 °C for 12 h. The product was cooled at room temperature and washed with ultrapure water 3 times. The white precursors were dried overnight at 60 °C. g-C₃N₄ nanostructures were also synthesized by

direct thermal polymerization, which was similar to the process of bulk g-C₃N₄. The final product was named G200.

2.4. Synthesis of Nano-NiTiO₃/g-C₃N₄ and Bulk-NiTiO₃/g-C₃N₄ Composite Catalysts

The nanostructures g-C₃N₄ and nano-NiTiO₃ were mixed according to a mass ratio of 1:1 and dissolved in 50 mL methanol. The mixture was treated with an ultrasonic crusher for 30 min and dried at 60 °C. The yellow products were heated at 400 °C for 2 h to synthesize nano-NiTiO₃/g-C₃N₄ composite catalysts. The bulk-NiTiO₃/g-C₃N₄ heterojunction was prepared using nano-NiTiO₃ and bulk g-C₃N₄. The synthetic method was similar to the process of nano-NiTiO₃/g-C₃N₄. The obtained nano-NiTiO₃/g-C₃N₄ heterojunction was named GN200, and the bulk-NiTiO₃/g-C₃N₄ heterojunction was named BGN.

2.5. Characterization

Field-emission scanning electron microscopy (SEM, Hitachi SU5000, Tokyo, Japan) was used to observe the morphology of the catalysts. The composition of nano-NiTiO₃/g-C₃N₄ (GN200) was determined by energy dispersive X-ray spectrometry (EDS, Oxford Instruments Ultim Max) attached to SEM. The crystalline structures of the catalyst were characterized using X-ray diffraction (XRD, Bruker D8 ADVANCE, Saarbrücken, Germany) with Cu K α radiation ($\lambda = 0.15406$ nm, scanning rate of 0.025°/s). X-ray photoelectron spectroscopy (XPS, Thermo Fisher K-Alpha, Waltham, MA, USA) was used to analyze the elemental composition of the catalyst. UV–vis diffuse reflection spectra (DRS) of the catalyst were examined on a UV-VIS-NIRs spectrophotometer (UV-3600Plus, Shimadzu, Kyoto, Japan) from 200 to 800 nm using BaSO₄ as a reference. In order to investigate the band gap of the catalyst, the UV–vis diffuse reflectance spectroscopy data were subjected to conversion using Formula (1).

$$(\alpha hv)^n = k(hv - E_g) \quad (1)$$

where α is the absorption index, h is the Planck constant, v is the frequency, E_g is the semiconductor band-gap width, and k is a constant. n is related to the type of semiconductor, which is 1/2 for the indirect transition.

The photoluminescence (PL) spectra were measured using a fluorescence spectrophotometer (F4600, Hitachi, Tokyo, Japan) with an excitation wavelength of 400 nm at 25 °C. The Brunauer–Emmett–Teller (BET) surface area of all of the samples prepared was obtained by being measured at liquid nitrogen temperature (Quantachrome Instruments, Boynton Beach, FL, USA). Samples were degassed at 300 °C for 6 h in a vacuum before testing. The photocurrent and Mott–Schottky curves were measured using a three-electrode system on an electrochemical workstation (CHI-660E, Chenhua, Shanghai, China).

2.6. Photocatalytic Activity Evaluation

The photocatalytic activities of the prepared catalyst were measured by the degradation of MB in an aqueous solution under visible light. A total of 50 mL of methylene blue aqueous solution (MB = 10 mg/L) was put into a quartz tube, and then 40 mg of catalyst was added to the solution. The suspension was stirred for 30 min under dark conditions to reach adsorption–desorption equilibrium. After reaching equilibrium, the solution was irradiated for 150 min using a 300 W xenon lamp (CEL-LAB500E4, Beijing, China) under visible light ($\lambda > 420$ nm) (Figure 1). The optical energy density of the xenon lamp was approximately 100 mW/cm². During the experiment, the photocatalytic system was cooled by a cooling water circulator (LX-2000, Beijing, China). Then, 0.5 mL of the mixture was collected from the solution every 30 min, and the sample was centrifuged to remove the photocatalyst. The MB concentration was measured at 665 nm by a UV–vis spectrophotometer (T6, Puxi, China). The degradation process of methylene blue conformed to the pseudo-first-order reaction kinetics equation by analyzing the relationship between the

photodecomposition time and the concentration of methylene blue in the solution. The reaction rate was calculated by Formula (2) (Pham, et al., 2018) [29]:

$$\ln(C_t/C_0) = kt \quad (2)$$

where k is the pseudo-first-order reaction kinetic rate constant, and C_0 and C_t are the initial concentration of MB solution and the remaining concentration of methylene blue in the solution at time t .



Figure 1. Photochemical reaction system.

2.7. Photocatalytic Mechanism Evaluation

The free radical capture test was used to study the photocatalytic mechanism. During the experiment, isopropyl alcohol (IPA, scavenger of $\cdot\text{OH}$), ethylenediamine tetraacetic acid sodium (EDTA-2Na, scavenger of h^+), and N_2 (eliminate oxygen) were added to MB aqueous solution. The experimental process was similar to photocatalytic degradation mentioned above.

3. Results and Discussion

3.1. Structure and Morphology of Photocatalysts

3.1.1. XRD Analysis

Figure 2 illustrates the XRD patterns of BG, NT, G200, BGN, and GN200. In the XRD pattern of BG depicted in Figure 2, two distinct diffraction peaks were observed at approximately $2\theta = 13.1^\circ$ and 27.5° , corresponding to the (100) and (002) diffraction planes of pure $\text{g-C}_3\text{N}_4$, as reported in the JCPDS 87–1526 database [30]. Notably, G200 and BG exhibited similar peak positions in the XRD pattern, but the (002) peak of G200 appeared weaker and broader compared to that of BG. A similar phenomenon has been observed in previous studies on $\text{g-C}_3\text{N}_4$ nanosheets, as reported by Huang et al. (2017) [31]. The XRD pattern of NT exhibited distinct diffraction peaks at 24.1° , 33.1° , 35.7° , 40.9° , 45.4° , 50.0° , 57.5° , 62.7° , and 64.2° , which corresponded to the (012), (104), (110), (113), (024), (116), (018), (214), and (300) diffraction planes of pure NiTiO_3 based on the JCPDS 33–0960 database [20]. No additional peaks related to TiO_2 or NiO were detected, indicating that NT consisted solely of pure NiTiO_3 with high crystallinity. The XRD patterns of BGN and GN200 displayed diffraction peaks corresponding to both $\text{g-C}_3\text{N}_4$ and NiTiO_3 , confirming the presence of $\text{g-C}_3\text{N}_4$ and NiTiO_3 in these composites. Comparing the XRD patterns of BGN and GN200 with those of BG, a significant reduction in the intensity of the diffraction

peaks at $2\theta = 27.5^\circ$ and 13.1° was observed. This reduction suggests that the hydrothermal treatment and ultrasonic crushing not only decreased the crystallinity of $g\text{-C}_3\text{N}_4$ but also successfully dispersed the agglomerated structure of $g\text{-C}_3\text{N}_4$ [32,33].

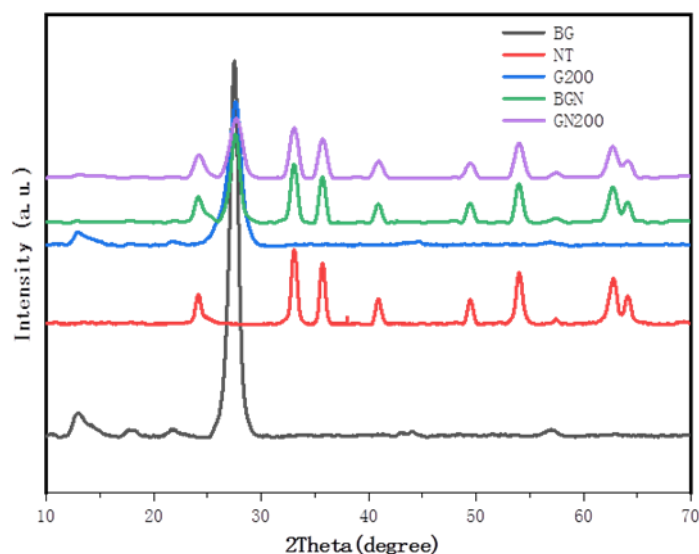


Figure 2. XRD patterns of BG, NT, G200, BGN, and GN200.

3.1.2. XPS Analysis

The elemental chemical states on the surface of the prepared catalyst were analyzed using XPS. The survey XPS spectra are presented in Figure 3a. In the case of bulk $g\text{-C}_3\text{N}_4$ (BG), the surface was predominantly composed of carbon (C) and nitrogen (N), with a small amount of oxygen (O) detected. For NT, the surface elements observed were titanium (Ti), nickel (Ni), and oxygen (O), along with a minor presence of carbon (C), potentially due to carbon contamination during sample preparation. The XPS spectra of G200 exhibited the presence of all of the elements from both NT and BG. Figure 3b displays the XPS spectra of the C 1s region for BG, BGN, and GN200. Peaks at 284.7 eV and 288.2 eV were observed in all three samples. The peak at 284.7 eV corresponds to sp^3 C-C bonds, while the peak at 288.2 eV corresponds to sp^2 N=C-N bonds, as reported in previous studies [6,34]. Furthermore, Figure 3c shows the XPS spectra of the N 1s region for BG, BGN, and GN200. Peaks at 398.8 eV, 400.4 eV, and 404.1 eV were observed in BG. These peaks are associated with sp^2 -hybridized N(C=N-C), C-N-H, and π excitation, respectively [35]. The peak at 404.1 eV was not observed in BGN and GN200, consistent with the findings of Huang et al., indicating a structural change in $g\text{-C}_3\text{N}_4$ when it forms a heterojunction with NiTiO_3 [26]. The banding energy of C=N-C groups at 404.1 eV disappeared, indicating that the $g\text{-C}_3\text{N}_4$ structure has changed feebly to form the heterojunction [36].

Figure 3d illustrates the XPS spectra of the Ni 2p region for BG, BGN, and GN200. Peaks at 855.6 eV, 862.0 eV, 873.3 eV, and 880.0 eV were observed in all three samples. The dominant peaks at approximately 855.6 eV and 873.3 eV correspond to the Ni 2p_{3/2} and Ni 2p_{1/2} states, respectively. The peaks at 862.0 eV and 880.0 eV are satellite peaks, which aligns with the findings of Kim et al. [36]. In addition, Figure 3e presents the XPS spectra of the Ti 2p region for BG, BGN, and GN200. Peaks at 458.2 eV, 458.8 eV, 463.9 eV, and 465.0 eV were observed in all three samples. The peaks of Ti 2p_{3/2} at 458.2 eV and 464.4 eV can be attributed to the oxidation state of Ti^{3+} , while those of Ti 2p_{1/2} at 458.8 eV and 465.0 eV can be assigned to the oxidation state of Ti^{4+} [17]. Notably, in the XPS spectra of BGN and GN200, a small peak appears at 460.6 eV, corresponding to the Ti-N peak [35]. This observation might explain why the peak at 404.1 eV in the N 1s region was not detected in BGN and GN200. Previous studies have indicated that Ti-N bridges have a significant impact on the photocatalytic activity of heterojunctions [18]. The ratio of $\text{Ti}^{3+}/\text{Ti}^{4+}$ in BGN and GN200 was found to be smaller compared to NT, suggesting that more Ti elements were bonded to $g\text{-C}_3\text{N}_4$ in the

heterojunction. Furthermore, the peak area at 460.6 eV in GN200 was significantly larger than that in BGN. This result implies that g-C₃N₄ prepared from melamine, treated by a hydrothermal method, exhibited a higher tendency to interact with Ti in the NiTiO₃ lattice, promoting the formation of a heterojunction.

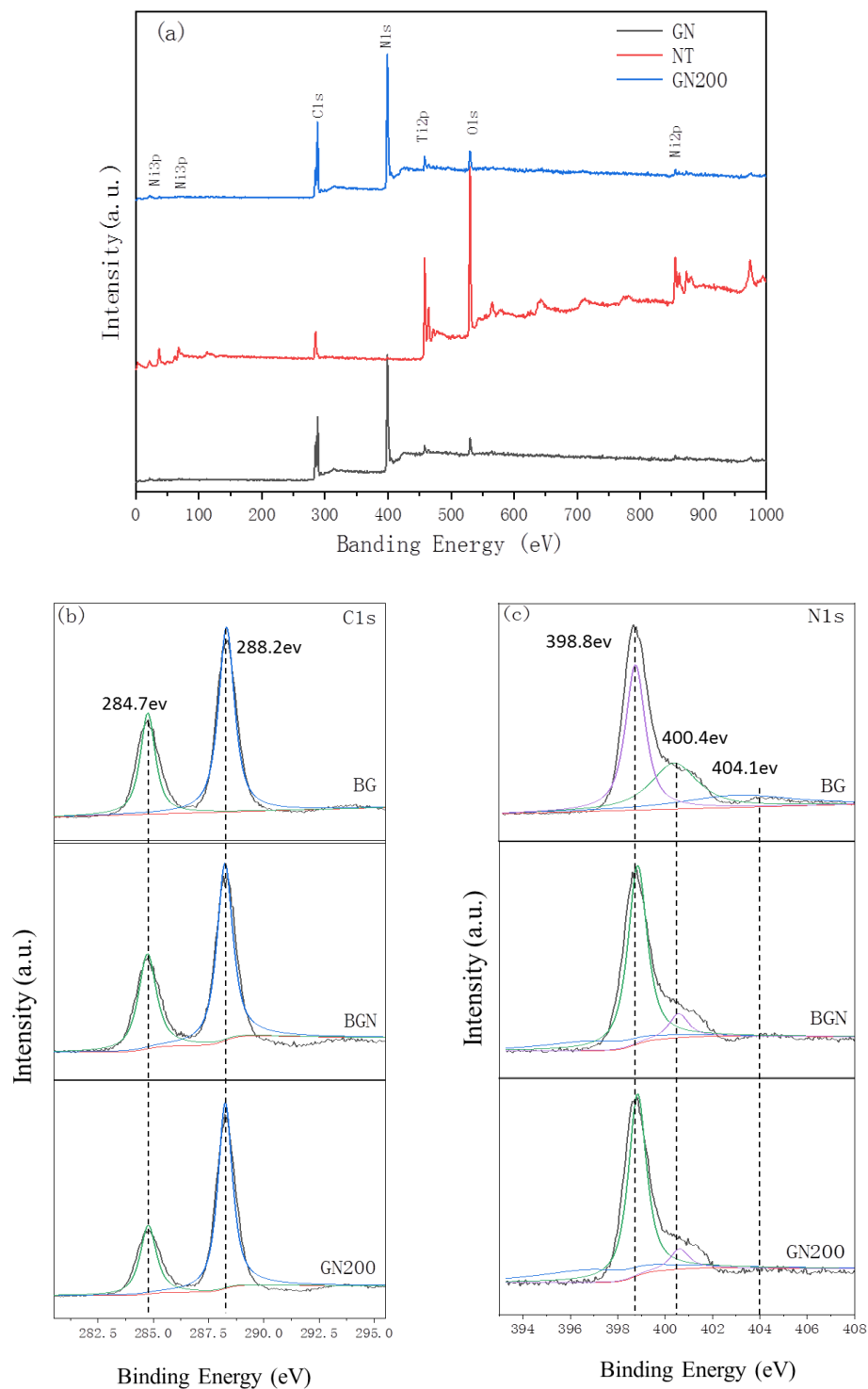


Figure 3. Cont.

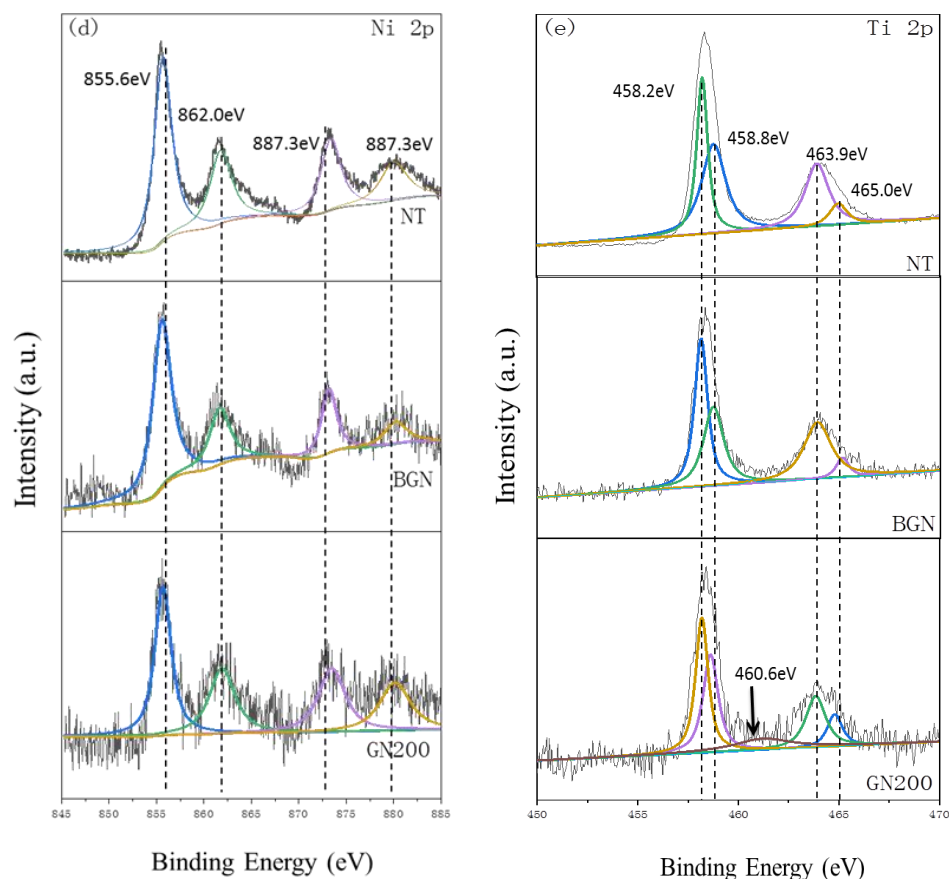


Figure 3. (a) XPS survey spectrum, (b) C1 s, (c) N1 s, (d) Ni 2p, and (e) Ti 2p.

3.1.3. Morphology

The morphologies of BG, NT, G200, BGN, and GN200 were examined using SEM, as shown in Figure 4. BG exhibited a large lamellar structure with a bulky size, which is characteristic of bulk $g\text{-C}_3\text{N}_4$ (Figure 4a) [20]. The morphology of pure NiTiO_3 appeared rod-like, with an average diameter ranging from approximately 1.5 to 2.5 μm (Figure 4b). In comparison, G200 exhibited a looser structure with fractures and pores on its surface, presenting a two-dimensional sheet structure (Figure 4c). Previous studies have suggested that during the hydrothermal process, some melamine undergoes hydrolysis and conversion into cyanuric acid. The resulting $g\text{-C}_3\text{N}_4$, obtained through direct thermal polymerization of melamine and cyanic acid, exhibited a bent and stripped morphology [35]. It is worth noting that the yield of $g\text{-C}_3\text{N}_4$ prepared through thermal oxidation of the hydrothermally pretreated mixture was approximately 2.1 times higher (13%) compared to the yield reported in previous studies (6%) [36]. In the case of BGN and GN200 samples, NT nanorods were observed to be attached to the surface of $g\text{-C}_3\text{N}_4$ (Figure 4d–f), indicating a strong interaction between NT and $g\text{-C}_3\text{N}_4$. The elemental mapping and EDS analyses of GN200 further confirmed the elemental composition of GN200, which consisted of C, N, Ti, Ni, and O (Figure 5). From HRTEM (Figure 6a), the BG had a compact granular structure, but G200, synthesized through thermal polymerization of melamine, had an obvious nanosheet structure, and the thickness of the nanosheets was about 15–20 nm (Figure 6c). Compared with the GB, the G200 had a larger specific surface area, which could provide more reaction sites when used as a catalyst. From HRTEM (Figure 6b), NT had a nanorod structure aggregated by nanoparticles. The NT in BGN was coated with $g\text{-C}_3\text{N}_4$ particles (BG) to form a rod-like heterojunction. However, the NT particles in GN200 were dispersed in the nanosheets, forming heterogeneous junctions with a larger specific surface area. And Figure 6 shows the lattice fringes of 0.36 and 0.25 nm, corresponding to the (012) and (110) crystallographic planes of ilmenite NiTiO_3 , respectively (Figure S5).

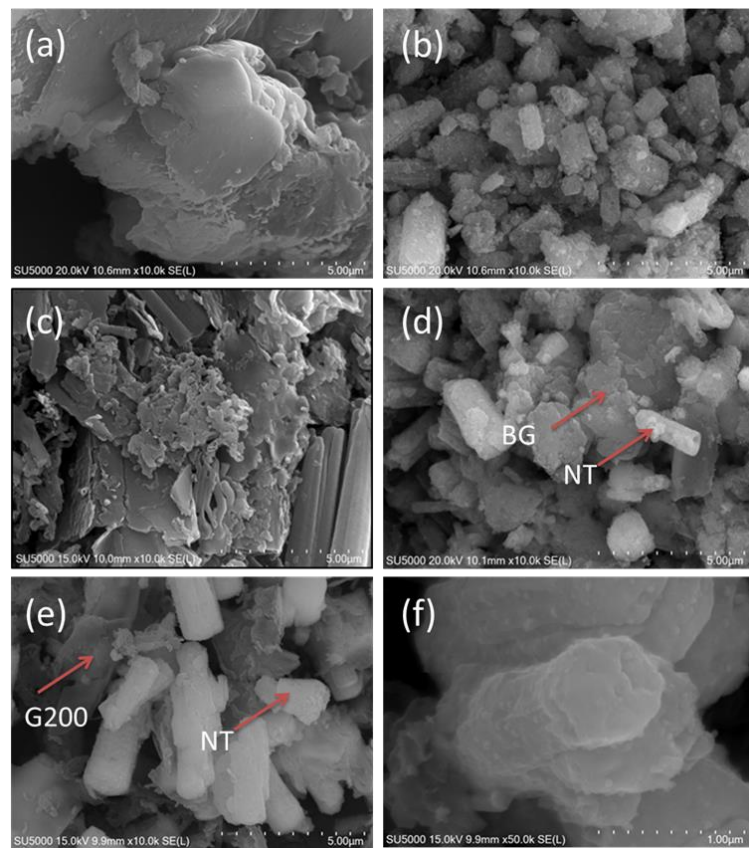


Figure 4. SEM images of (a) BG, (b) NT, (c) G200, (d) BGN, and (e,f) GN200.

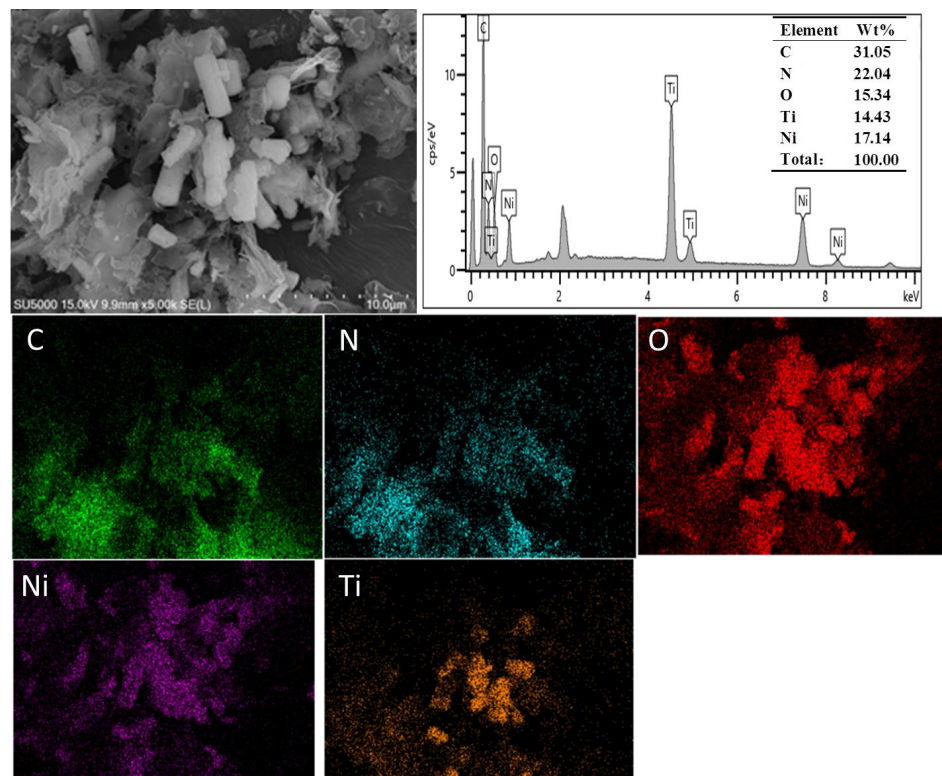


Figure 5. EDS and elemental mapping patterns of GN200.

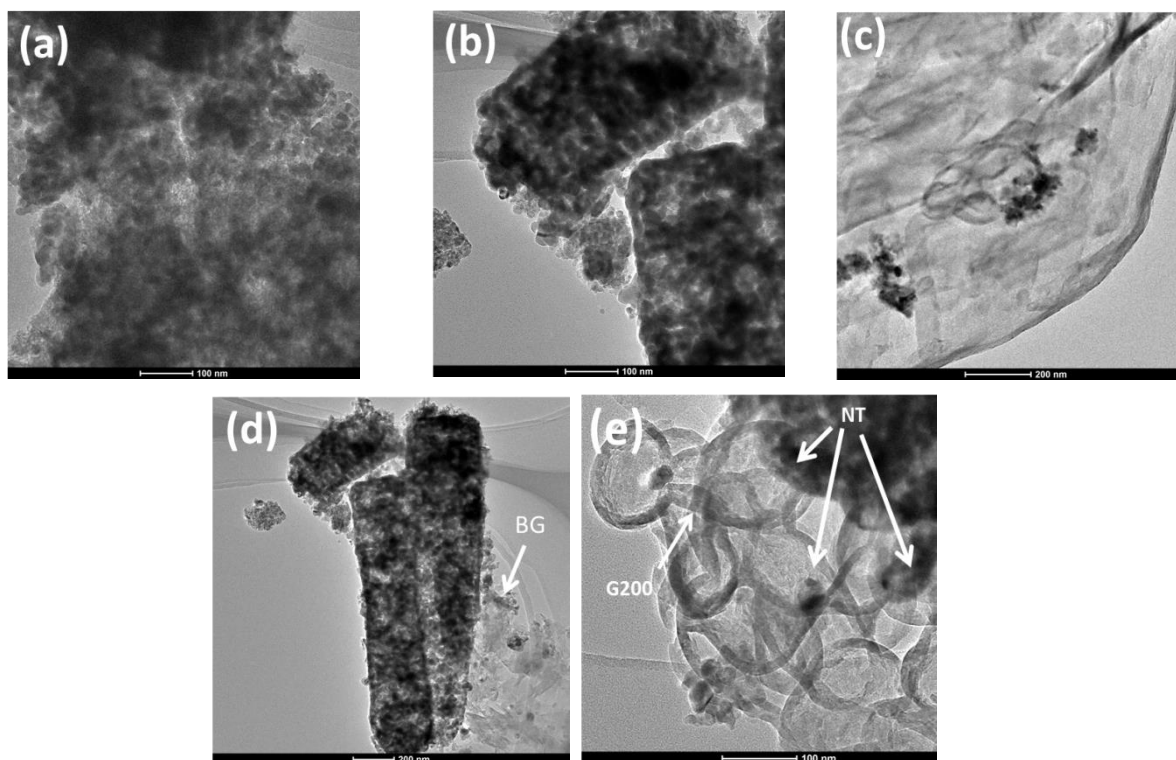


Figure 6. HRTEM images of (a) BG; (b) NT; (c) G200; (d) BGN; (e) GN200.

3.1.4. Brunauer–Emmett–Teller and Adsorption Capacities

The Brunauer–Emmett–Teller (BET) surface areas of BG, NT, BGN, and GN200 were determined using adsorption–desorption techniques, as depicted in Figure 7a. The hysteresis loops observed in the adsorption–desorption curves of all samples, as shown in Figure 7a, indicate the presence of mesoporous structures [37]. The BET surface area of BG was a mere $11.90 \text{ m}^2/\text{g}$, while that of G200 was significantly higher at $36.55 \text{ m}^2/\text{g}$ (see Supplementary Data, Figure S1a). This marked increase in BET surface area for BGN and GN200, compared to BG and G200, suggests that the formation of heterojunctions can enhance the specific surface area of $g\text{-C}_3\text{N}_4$. The specific surface areas of NT and G200 synthesized in this paper were 2.3–4.7 times and 3.6–7.8 times those obtained by the traditional methods, respectively, and the specific surface area of GN200 synthesized by a two-step method was 1.6–2.2 times that of the other studies [17,24–27,37]. Consequently, these findings imply that nanostructured $g\text{-C}_3\text{N}_4$ and nanostructured heterojunctions possess a substantial specific surface area, which in turn provides a greater number of adsorption sites and photocatalytic activity sites. Figure 7b illustrates the adsorption characteristics of the four catalysts for methylene blue, and the adsorption process of the catalyst for methylene blue aligns with the quasi-second-order kinetic model. The quasi-second-order kinetic equation was employed to calculate the maximum adsorption quantity (q_e) [22]. The maximum adsorption capacities of the four catalysts are summarized in the table presented in Figure 7b. The adsorption capacities of NT and BG for methylene blue exhibited similarity, while GN200 and BGN demonstrated 2.0 and 1.7 times higher adsorption capacities than BG, respectively. These findings are consistent with the study conducted by Qu et al. [17]. Further support for this observation can be found in Figure S1b of the Supplementary Data, which indicates that GN200 not only possesses a larger specific surface area compared to the other three catalysts but also exhibits a more abundant pore size structure, thereby facilitating the adsorption of MB. Some studies have found that the BET total specific surface area was not the key factor affecting the adsorption of methylene blue, but the range of mesoporous size range was the superior pore size for MB adsorption [38].

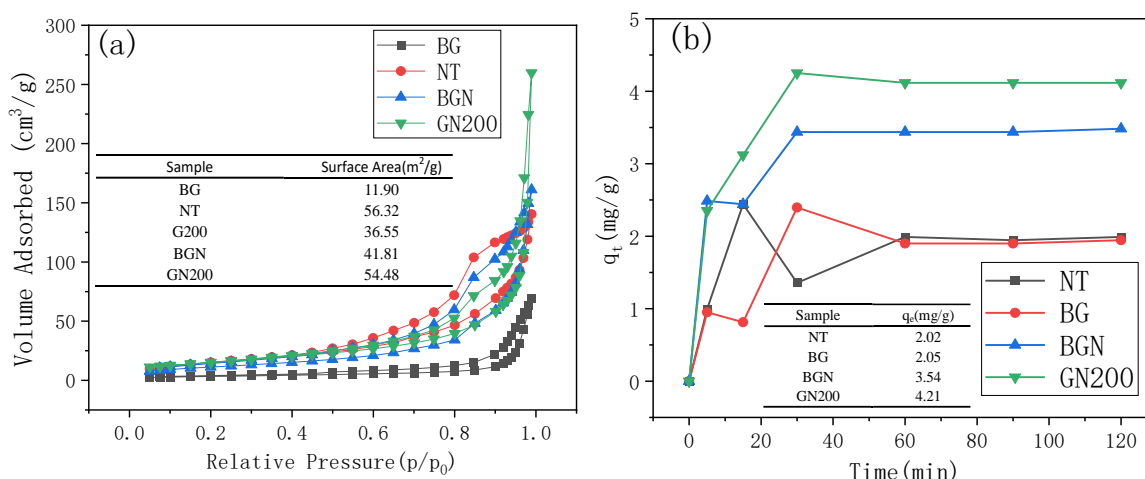


Figure 7. (a) N₂ adsorption–desorption isotherms; (b) adsorption of catalyst in the dark.

3.2. Photoelectric Property

3.2.1. UV–Vis Absorption Spectra

UV–vis diffuse reflectance spectroscopy was employed to ascertain the spectral absorption range and band gap of the four catalysts, as depicted in Figure 8a. The results revealed that all four catalysts exhibited broad absorption capabilities within the visible light range, suggesting their suitability as visible light catalytic materials. The initial absorption wavelength for BG was determined to be 484 nm. Notably, NT displayed two absorption peaks at 514 nm and 546 nm, which align with the absorption characteristics of nanostructured NiTiO₃ [39]. According to theoretical calculations, the band gaps of BG and NT are 2.43 eV and 1.64 eV, respectively, and that of G200 is 2.20 eV (Supplementary Data Figure S3a). The band gaps of BGN and GN200 are 1.87 eV and 2.27 eV, respectively (Figure 8b). According to the band gap of the prepared catalyst, all of them can be used for visible light catalytic reactions.

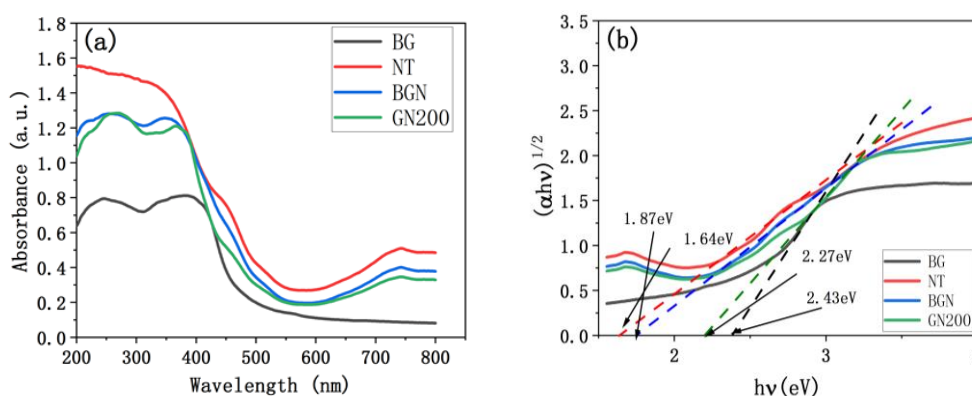


Figure 8. (a) UV–visible diffuse reflectance spectroscopy of the catalyst; (b) calculated band gap of the catalyst.

3.2.2. Photoluminescence Spectra

Photoluminescence (PL) emission spectra are commonly used to characterize the recombination rate of photogenerated holes and photogenerated electrons in photocatalysis when subjected to photoexcitation. Figure S2a displays the PL emission spectra of BG, G200, BGN, and GN200 at 350 nm. The PL emission peak of the heterojunction (BGN and GN200) exhibited a noticeable blueshift compared to that of pure g-C₃N₄, and the blueshift of the PL emission peak was more pronounced in GN200 compared to BG. This observation suggests that the quantum effect on the nanostructure contributes to the blueshift of the PL

emission peak [40]. Additionally, the PL emission peak of G200 was lower than that of BG, indicating that the 2D $g\text{-C}_3\text{N}_4$ nanosheet structure effectively reduces the recombination rate of photogenerated electrons and holes, aligning with the findings of Yang et al. [41]. Among the four catalysts, GN200 displayed the lowest PL emission intensity, indicating a lower photocarrier load rate. This finding is supported by the transient photocurrent response of the photocatalyst (Figure S2b). The photoelectric conversion efficiency of BG, BGN, and GN200 is shown in the attached Supplementary Data (Table S1). It has been shown that the photoelectric conversion efficiency of GN200 was 1.3%, which was 21 times that of BG and 1.4 times that of BGN. Some studies have shown that the construction of nanostructured heterojunctions could improve the PCE of photocatalysts [42].

3.2.3. Mott–Schottky Analysis

The properties of the valence band (VB) and conduction band (CB) have a significant impact on the recombination mode of holes and electrons as well as the oxidation–reduction capabilities of the photocatalyst, as mentioned by Yang et al. [41]. Therefore, in order to understand the band structure of G200 and NT, Mott–Schottky (MS) analysis was performed (refer to Figure 9), enabling the estimation of the CB edge (ECB) for both G200 and NT. The MS plots display positive slopes, indicating that both NT and G200 exhibited characteristics of n-type semiconductors, as observed by Sun et al. [43]. The calculation revealed that the flat bands (CFB) for G200 and NT were -1.61 eV and -0.34 eV, respectively, relative to Ag/AgCl. In the case of n-type semiconductors, the ECB typically was approximately 0.1 eV below the EFB. Consequently, the ECB values for G200 and NT were approximately -1.51 eV and -0.24 eV, respectively. Using the equation $E_{VB} = E_g + E_{CB}$, along with the band gap results from Figure 7b, the EVB values for G200 and NT were determined as 0.69 eV and 1.40 eV, respectively, relative to NHE. According to Figure S3b, it can be inferred that the CB potential of G200 was more negative compared to BG (-1.32 eV), thereby facilitating photocatalysis for the reduction of O_2 to $\cdot\text{O}_2^-$ (-0.33 eV), as described by Zhang et al. [44].

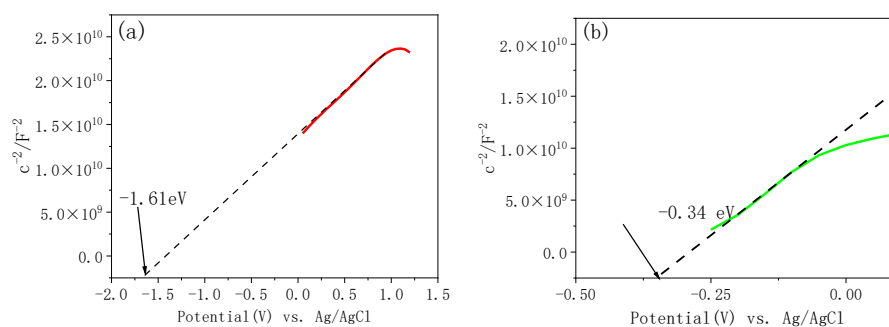


Figure 9. Mott–Schottky plots of (a) G200 and (b) NT.

3.3. Photocatalytic Evaluation

The degradation efficiencies of BG, NT, BGN, and BG200 for methylene blue under simulated visible light (optical density = 35–40 mW/cm^2 , CEL-NP2000–2, Beijing, China) were measured (Figure 10a,b). Figure 10a illustrates the photodegradation rate of methylene blue (MB) by the four catalysts, with GN200 exhibiting the highest photodegradation rate (98%), followed by BGN (67%), BG (59%), and NT (36%). The reaction rate was calculated by Formula (2), and the results are shown in Figure 10b. Figure 10b illustrates the degradation rate of methylene blue (MB) by the four catalysts, with GN200 exhibiting the highest degradation rate (0.0156 min^{-1}), followed by BGN (0.0072 min^{-1}), BG (0.0062 min^{-1}), and NT (0.0033 min^{-1}). These results indicate that the photocatalytic properties of BGN and GN200 surpass those of NT and BG, suggesting the formation of a $\text{NiTiO}_3/g\text{-C}_3\text{N}_4$ heterojunction. The photodegradation rate of methylene blue by GN200 was 2.5–19.7 times that of $\text{NiTiO}_3/g\text{-C}_3\text{N}_4$ synthesized by other methods [36,44]. The notable enhancement in

catalytic performance observed in GN200 can be attributed to its richer pore size structure, which facilitates the entry of MB molecules into the catalyst and promotes degradation. Additionally, Figure 3e demonstrates that GN200 possesses more Ti-N bonds compared to BGN. It has been observed that the catalytic activity of the heterojunction is closely linked to internal Ti-N bonds, which contribute to the improved catalytic activity [45]. To validate the catalytic stability and repeatability of the GN200 catalyst, cyclic photodegradation experiments were conducted under the same conditions. Following each cycle of the experiment, the catalyst was recovered and cleaned using alcohol and deionized water. The results indicate that the catalytic performance of GN200 experienced a slight decrease of 1.2% after four repeated tests, signifying good catalytic stability (Figure S4).

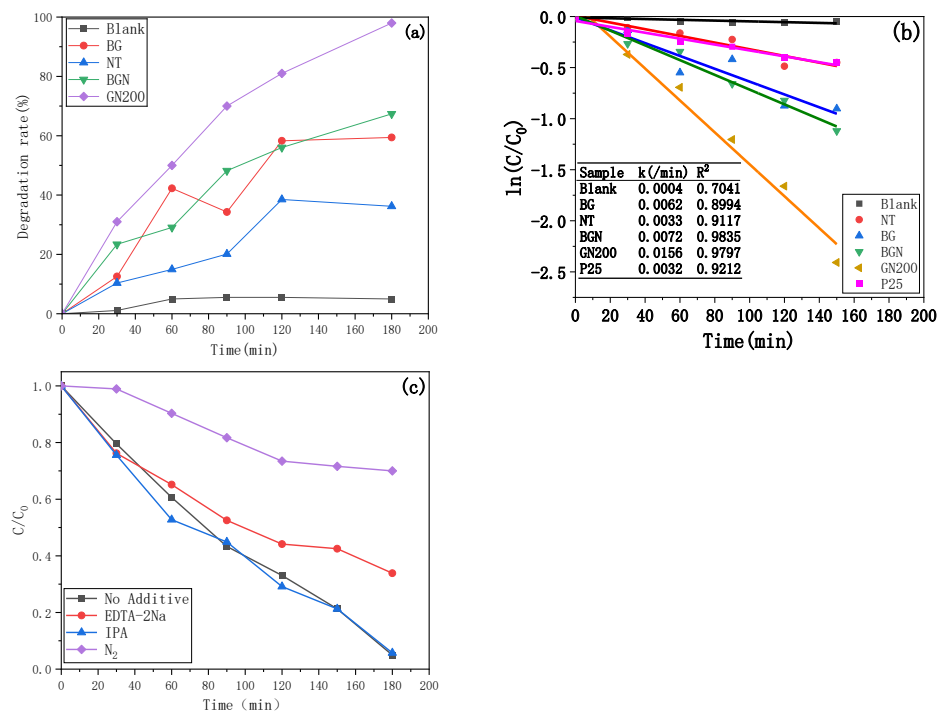


Figure 10. (a) Photodegradation curves of MB with BG, NT, BGN, and BG200; (b) photocatalytic degradation rate of MB with BG, NT, BGN, and BG200; (c) trapping test of free radicals during degradation for the photodegradation of MB on sample GN200.

The investigation of active compounds involved in the degradation of MB was conducted by introducing free radical and void-trapping agents into the experimental setup. As illustrated in Figure 10c, the addition of isopropanol (IPA) had a negligible impact on the degradation rate of MB, which was about 94.3%, thus suggesting that $\cdot\text{OH}$ had minimal influence on the process of MB degradation. The addition of EDTA-2Na only slightly diminished the degradation rate of MB, which was about 66.1%, indicating that holes (h^+) played a role in the MB degradation process. Moreover, when O_2 was eliminated from the reaction system through the introduction of N_2 , the degradation rate of MB was about 30.1%. This strongly suggests that $\cdot\text{O}_2^-$, generated by O_2 , played a crucial role in the degradation of MB.

3.4. Photocatalytic Mechanisms

The determined band gaps of G200 and NT suggest that both materials are capable of being excited by absorbing visible light. In the case of GN200, if a double-charge transfer mechanism is followed, the photogenerated electrons in G200 would migrate to the conduction band (CB) of NT. Given that the standard redox potential of the NT CB potential (-0.24 eV) is higher than that of $\text{O}_2/\cdot\text{O}_2^-$ (-0.33 eV), the formation of $\cdot\text{O}_2^-$ is hindered. As depicted in Figure 11, the potentials of the G200 valence band (VB)

(0.69 eV) and NT (VB) (1.4 eV) are both lower than those of $\text{OH}^-/\cdot\text{OH}$ (1.90 eV) and $\text{H}_2\text{O}/\cdot\text{OH}$ (2.70 eV) [44,46]. Consequently, the production of $\cdot\text{OH}$ at the VB edge of G200 and NT is not feasible, thereby explaining why the addition of isopropyl alcohol has no impact on MB degradation. On the other hand, the potential of G200 CB (-1.57 eV) is lower than that of $\text{O}_2/\cdot\text{O}_2^-$ (-0.33 eV), allowing the electrons generated in the G200 CB to capture O_2 and generate $\cdot\text{O}_2^-$. This outcome indicates that the electrons produced by the NT CB in the heterojunction can only migrate toward the G200 VB, supporting the hypothesis that GN200 operates according to a Z-scheme-type mechanism. Figure S3b demonstrates that BG is also an n-type semiconductor with a flat band of -1.42 eV, relative to Ag/AgCl, resulting in an ECB and EVB of -1.32 eV and 1.11 eV, respectively. Since the potential of G200 CB is more negative than that of BG, the reduction capacity of the heterojunction is significantly enhanced [46], which aligns with the highest degradation efficiency observed in GN200.

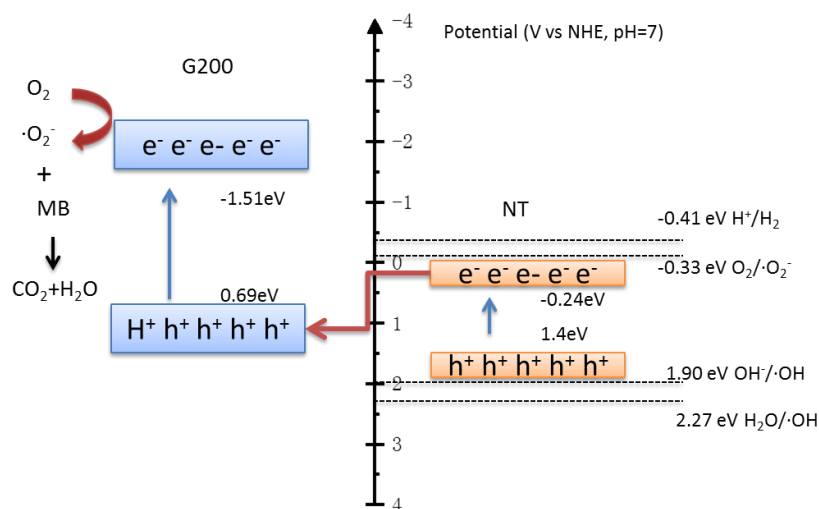


Figure 11. Proposed mechanism of GN200 degradation for MB under visible light irradiation.

4. Conclusions

In this study, we showed that the specific surface area and photocatalytic performance of the photocatalyst can be significantly improved by optimizing the preparation method of the photocatalyst precursor. A nano- $\text{NiTiO}_3/\text{g-C}_3\text{N}_4$ photocatalyst was successfully synthesized with a two-step method. Compared with previously studies, the specific surface area of the novel material was increased by 1.6–2.2 times. According to the pseudo-first-order, the degradation rate of MB was more than 2.5–19.7 times higher than that of previously studies, which was attributed to the improvement in the carrier separation capability and the acceleration of the charge transfer. The radical scavenging experiments showed that $\cdot\text{O}_2^-$ and holes (h^+) played significant roles in the photocatalytic reaction of methylene blue (MB). Cycled experiments demonstrated that a nano- $\text{NiTiO}_3/\text{g-C}_3\text{N}_4$ photocatalyst could maintain more than a 90% MB removal rate after four rounds of recycling. This work opens a new avenue for the synthesis of photocatalysts.

Supplementary Materials: The following supporting information can be downloaded at: <https://www.mdpi.com/article/10.3390/separations11030077/s1>, Figure S1. (a) N_2 adsorption-desorption isotherms of G200; (b) Barret–Joyner–Halenda (BJH) pore-size distribution of BG, NT, BGN and GN200; Figure S2. (a) PL spectra of the photocatalyst; (b) transient photocurrent responses of the photocatalyst; Figure S3. (a) Calculated band gap of G200; (b) Mott–Schottky plots of BG.; Figure S4. Degradation performance of GN200 toward MB over four cycles; Figure S5. HRTEM image of GN200; Table S1. Photoelectric conversion efficiency (PCE) of BG, BGN and GN200; Ref. [47] is cited in Supplementary Materials.

Author Contributions: L.S., J.D. and A.Q.: supervision, writing, reviewing, and editing. D.L. and H.R.: conceived, designed, and conducted the study, analyzed the experimental data, and wrote the original draft. K.W., L.Z. and Z.Y.: funding acquisition and project administration. All authors have read and agreed to the published version of the manuscript.

Funding: This study was funded by open access funding enabled and organized by the Integration of Science, Education and Industry Innovation Pilot Project of Qilu University of Technology (Shandong Academy of Sciences) (2020KJC-ZD12), ShanDong students' innovation and entrepreneurship training program (S202010431063), and the talent and scientific research project of Qilu University of Technology (No. 11240850).

Data Availability Statement: All relevant data are within the paper.

Acknowledgments: We acknowledge support from the National Engineering Laboratory for Lake Pollution Control and Ecological Restoration, the State Environment Protection Key Laboratory for Lake Pollution Control, Chinese Research Academy of Environmental Sciences, Beijing 100012, China, and the School of Environmental Science and Engineering, Qilu University of Technology (Shandong Academy of Sciences), Jinan, China.

Conflicts of Interest: The authors declare no conflicts of interest.

References

1. Wang, S.; Han, X.; Zhang, Y.; Tian, N.; Ma, T.; Huang, H. Inside-and-out Semiconductor Engineering for CO₂ Photoreduction: From Recent Advances to New Trends. *Small Struct.* **2020**, *2*, 2000061. [[CrossRef](#)]
2. Chen, X.; Shen, S.; Guo, L.; Mao, S.S. Semiconductor-based Photocatalytic Hydrogen Generation. *Chem. Rev.* **2010**, *110*, 6503–6570. [[CrossRef](#)]
3. Ong, W.J.; Tan, L.L.; Ng, Y.H.; Yong, S.T.; Chai, S.P. Graphitic Carbon Nitride (g-C₃N₄)-Based Photocatalysts for Artificial Photosynthesis and Environmental Remediation: Are We a Step Closer to Achieving Sustainability? *Chem. Rev.* **2016**, *116*, 7159–7329. [[CrossRef](#)] [[PubMed](#)]
4. Liu, J.; Wang, H.; Antonietti, M. Graphitic nitride “reloaded”: Emerging applications beyond (photo)catalysis. *Chem. Soc. Rev.* **2016**, *45*, 2308. [[CrossRef](#)] [[PubMed](#)]
5. Zhao, Z.; Sun, Y.; Dong, F. Graphitic carbon nitride based nanocomposites: A review. *Nanoscale* **2014**, *7*, 15–37. [[CrossRef](#)] [[PubMed](#)]
6. Zeng, Y.P.; Wang, Y.; Chen, J.W.; Jiang, Y.W.; Kiani, M.; Li, B.Q.; Wang, R.L. Fabrication of High-activity Hybrid NiTiO₃/g-C₃N₄ Heterostructured Photocatalysts for Water Splitting to Enhanced Hydrogen Production. *Ceram. Int.* **2016**, *42*, 12297–12305. [[CrossRef](#)]
7. Ye, R.Q.; Fang, H.B.; Zheng, Y.Z.; Li, N.; Wang, Y.; Tao, X. Fabrication of CoTiO₃/g-C₃N₄ Hybrid Photocatalysts with Enhanced H₂ Evolution: Z-Scheme Photocatalytic Mechanism Insight. *ACS Appl. Mater. Interfaces* **2016**, *8*, 13879–13889. [[CrossRef](#)] [[PubMed](#)]
8. Han, Q.; Wang, B.; Zhao, Y.; Hu, C.G.; Qu, L.T. A Graphitic-C₃N₄ “Seaweed” Architecture for Enhanced Hydrogen Evolution. *Angew. Chem.* **2015**, *54*, 11595–11599. [[CrossRef](#)]
9. Xu, J.; Zhang, L.; Shi, R.; Zhu, Y. Chemical exfoliation of graphitic carbon nitride for efficient heterogeneous photocatalysis. *J. Mater. Chem. A* **2013**, *1*, 14766–14772. [[CrossRef](#)]
10. Yang, J.; Zhang, X.Q.; Xie, C.F.; Long, J.Q.; Wang, Y.Q.; Wei, L.; Yang, X.D. Preparation of g-C₃N₄ with high specific surface area and photocatalytic stability. *J. Electron. Mater.* **2021**, *55*, 1067–1074. [[CrossRef](#)]
11. Groenewolt, M.; Antonietti, M. Synthesis of g-C₃N₄ Nanoparticles in Mesoporous Silica Host Matrices. *Adv. Mater.* **2005**, *17*, 1789–1792. [[CrossRef](#)]
12. Shi, W.; Song, S.; Zhang, H. Hydrothermal synthetic strategies of inorganic semiconducting nanostructures. *Chem. Soc. Rev.* **2013**, *42*, 5714–5743. [[CrossRef](#)] [[PubMed](#)]
13. Hong, Y.; Li, C.; Fang, Z.; Luo, B.; Shi, W. Rational synthesis of ultrathin graphitic carbon nitride nanosheets for efficient photocatalytic hydrogen evolution. *Carbon* **2017**, *121*, 463–471. [[CrossRef](#)]
14. Jung, H.; Pham, T.T.; Shin, E.W. Interactions between ZnO nanoparticles and amorphous g-C₃N₄ nanosheets in thermal formation of g-C₃N₄/ZnO composite materials: The annealing temperature effect. *Appl. Surf. Sci.* **2018**, *458*, 369–381. [[CrossRef](#)]
15. Gu, L.; Wang, J.; Zou, Z.; Han, X. Graphitic-C₃N₄-Hybridized TiO₂ Nanosheets with Reactive {001} Facets to Enhance the UV-And Visible-Light Photocatalytic Activity. *J. Hazard. Mater.* **2014**, *268*, 216–223. [[CrossRef](#)] [[PubMed](#)]
16. Fu, J.; Chang, B.; Tian, Y.; Xi, F.; Dong, X. Novel C₃N₄-CdS Composite Photocatalysts with Organic Inorganic Heterojunctions: In Situ Synthesis, Exceptional Activity, High Stability and Photocatalytic Mechanism. *J. Mater. Chem. A* **2013**, *1*, 3083–3090. [[CrossRef](#)]
17. Qu, Y.; Zhou, W.; Ren, Z.R.; Du, S.; Meng, X.; Tian, G.; Pan, K.; Wang, G.; Fu, H. Facile preparation of porous NiTiO₃ nanorods with enhanced visible-light-driven photocatalytic performance. *J. Mater. Chem.* **2012**, *22*, 16471–16476. [[CrossRef](#)]
18. Inceesungvorn, B.; Teeranunpong, T.; Nunkaew, J.; Suntalelat, S.; Tantraviwat, D. Novel NiTiO₃/Ag₃VO₄ composite with enhanced photocatalytic performance under visible light. *Catal. Commun.* **2014**, *54*, 35–38. [[CrossRef](#)]

19. Wang, X.; Maeda, K.; Thomas, A.; Takanabe, K.; Xin, G.; Carlsson, J.M.; Domen, K.; Antonietti, M. A metal-free polymeric photocatalyst for hydrogen production from water under visible light. *Nat. Mater.* **2009**, *8*, 76–80. [[CrossRef](#)]
20. Qu, Y.; Zhou, W.; Jiang, L.; Fu, H. Novel heterogeneous CdS nanoparticles/NiTiO₃ nanorods with enhanced visible-light-driven photocatalytic activity. *RSC Adv.* **2013**, *3*, 18305–18310. [[CrossRef](#)]
21. Jiang, L.; Yuan, X.; Pan, Y.; Liang, J.; Zeng, G.; Wu, Z.; Wang, H. Doping of graphitic carbon nitride for photocatalysis: A review. *Appl. Catal. B Environ.* **2017**, *217*, 388–406. [[CrossRef](#)]
22. Wang, H.; Yuan, X.; Wang, H.; Chen, X.; Wu, Z.; Jiang, L.; Xiong, W.; Zhang, Y.; Zeng, G. One-step calcination method for synthesis of mesoporous g-C₃N₄/NiTiO₃ heterostructure photocatalyst with improved visible light photoactivity. *RSC Adv.* **2015**, *5*, 95643–95648. [[CrossRef](#)]
23. Yuan, P.-H.; Fan, C.-M.; Ding, G.-Y.; Wang, Y.-F.; Zhang, X.-C. Preparation and photocatalytic properties of ilmenite NiTiO₃ powders for degradation of humic acid in water. *Int. J. Miner. Met. Mater.* **2012**, *19*, 372–376. [[CrossRef](#)]
24. Huang, Z.; Zeng, X.; Li, K.; Gao, S.; Wang, Q.; Lu, J. Z-scheme NiTiO₃/g-C₃N₄ heterojunctions with enhanced photoelectrochemical and photocatalytic performances under visible LED light irradiation. *ACS Appl. Mater. Interfaces* **2017**, *9*, 41120–41125. [[CrossRef](#)] [[PubMed](#)]
25. Wang, J.; Gao, B.; Dou, M.; Huang, X.; Ma, Z. A porous g-C₃N₄ nanosheets containing nitrogen defects for enhanced photocatalytic removal meropenem: Mechanism, degradation pathway and DFT calculation. *Environ. Res.* **2020**, *184*, 109339. [[CrossRef](#)] [[PubMed](#)]
26. Liang, Q.; Jin, J.; Liu, C.; Xu, S.; Yao, C.; Chen, Z.; Li, Z. Hydrothermal fabrication of alpha-SnWO₄/C₃N₄ heterostructure with enhanced visible-light photocatalytic activity. *J. Mater. Sci. Mater. Electron.* **2017**, *28*, 11279–11283. [[CrossRef](#)]
27. Huang, T.; Pan, S.; Shi, L.; Yu, A.; Wang, X.; Fu, Y. Hollow porous prismatic graphitic carbon nitride with nitrogen vacancies and oxygen doping: A high-performance visible light-driven catalyst for nitrogen fixation. *Nanoscale* **2019**, *12*, 1833–1841. [[CrossRef](#)] [[PubMed](#)]
28. Duan, X.Y.; Xu, J.H.; He, M.Q.; Zhang, X.Q. Preparation of 2D graphite phase carbon nitride nanosheets and their photocatalytic performance. *Fine Chem.* **2021**, *1*, 83–90.
29. Pham, T.-T.; Nguyen-Huy, C.; Lee, H.-J.; Nguyen-Phan, T.-D.; Son, T.-H.; Kim, C.-K.; Shin, E.-W. Cu-doped TiO₂/reduced graphene oxide thin-film photocatalysts: Effect of Cu content upon methylene blue removal in water. *Ceram. Int.* **2015**, *41*, 11184–11193. [[CrossRef](#)]
30. Zang, Y.P.; Li, L.P.; Li, X.G.; Lin, R.; Li, G.S. Synergistic Collaboration of g-C₃N₄/SnO₂ Composites for Enhanced Visible-light Photocatalytic Activity. *Chem. Eng. J.* **2014**, *246*, 277–286. [[CrossRef](#)]
31. Lin, Q.; Li, L.; Liang, S.; Liu, M.; Bi, J.; Wu, L. Efficient synthesis of monolayer carbon nitride 2D nanosheet with tunable concentration and enhanced visible-light photocatalytic activities. *Appl. Catal. B Environ.* **2015**, *163*, 135–142. [[CrossRef](#)]
32. Ding, W.; Liu, S.; He, Z. One-step synthesis of graphitic carbon nitride nanosheets for efficient catalysis of phenol removal under visible light. *Chin. J. Catal.* **2017**, *38*, 1711–1718. [[CrossRef](#)]
33. Nguyen, T.K.A.; Pham, T.-T.; Nguyen-Phu, H.; Shin, E.W. The effect of graphitic carbon nitride precursors on the photocatalytic dye degradation of water-dispersible graphitic carbon nitride photocatalysts. *Appl. Surf. Sci.* **2020**, *537*, 148027. [[CrossRef](#)]
34. Pham, T.T.; Shin, E.W. Influence of g-C₃N₄ Precursors in g-C₃N₄/NiTiO₃ Composites on Photocatalytic Behavior and the Interconnection between g-C₃N₄ and NiTiO₃. *Langmuir* **2018**, *34*, 13144–13154. [[CrossRef](#)] [[PubMed](#)]
35. Kim, S.-R.; Jo, W.-K. Application of a photostable silver-assisted Z-scheme NiTiO₃ nanorod/g-C₃N₄ nanocomposite for efficient hydrogen generation. *Int. J. Hydrogen Energy* **2018**, *44*, 801–808. [[CrossRef](#)]
36. Wang, X.J.; Yang, W.Y.; Li, F.T.; Xue, Y.B.; Liu, R.H.; Hao, Y.J. In Situ Microwave-assisted Synthesis of Porous NiTiO₃/g-C₃N₄ Heterojunctions with Enhanced Visible-light Photocatalytic Properties. *Ind. Eng. Chem. Res.* **2013**, *52*, 17140–17150. [[CrossRef](#)]
37. Oktay, S.; Kahraman, Z.; Urgen, M.; Kazmanli, K. XPS investigations of trilayers formed on Ti-N and (Ti,Re)N coatings. *Appl. Surf. Sci.* **2015**, *328*, 255–261. [[CrossRef](#)]
38. Ighalo, J.O.; Iwuozor, K.O.; Igwegbe, C.A.; Adeniyi, A.G. Verification of pore size effect on aqueous-phase adsorption kinetics: A case study of methylene blue. *Colloids Surf. A Physicochem. Eng. Asp.* **2021**, *626*, 127119. [[CrossRef](#)]
39. Zheng, J.; Lei, Z. Incorporation of CoO nanoparticles in 3D marigold flower-like hierarchical architecture MnCo₂O₄ for highly boosting solar light photo-oxidation and reduction ability. *Appl. Catal. B Environ.* **2018**, *237*, 1–8. [[CrossRef](#)]
40. Yang, B.; Wang, Z.; Zhao, J.; Sun, X.; Wang, R.; Liao, G.; Jia, X. 1D/2D carbon-doped nanowire/ultra-thin nanosheet g-C₃N₄ isotype heterojunction for effective and durable photocatalytic H₂ evolution. *Int. J. Hydrogen Energy* **2021**, *46*, 25436–25447. [[CrossRef](#)]
41. Luo, J.; Steier, L.; Son, M.K.; Schreier, M.; Mayer, M.T.; Grätzel, M. Cu₂O nanowire photocathodes for efficient and durable solar water splitting. *Nano Lett.* **2016**, *16*, 1848–1857. [[CrossRef](#)] [[PubMed](#)]
42. Sun, H.; Zhou, G.; Wang, Y.; Suvorova, A.; Wang, S. A New Metal-Free Carbon Hybrid for Enhanced Photocatalysis. *ACS Appl. Mater. Interfaces* **2014**, *6*, 16745–16754. [[CrossRef](#)] [[PubMed](#)]
43. Zhang, F.J.; Xie, F.Z.; Zhu, S.F.; Liu, J.; Zhang, J.; Mei, S.F.; Zhao, W. A Novel Photofunctional g-C₃N₄/Ag₃PO₄ Bulk Heterojunction for Decolorization of RhB. *Chem. Eng. J.* **2013**, *228*, 435–441. [[CrossRef](#)]
44. Dao, D.Q.; Nguyen, T.K.A.; Pham, T.T.; Shin, E.W. Synergistic effect on photocatalytic activity of co-doped NiTiO₃/g-C₃N₄ composites under visible light irradiation. *Catalysts* **2020**, *10*, 1332. [[CrossRef](#)]

45. Zheng, D.; Pang, C.; Liu, Y.; Wang, X. Shell-engineering of hollow g-C₃N₄ nanospheres via copolymerization for photocatalytic hydrogen evolution. *Chem. Commun.* **2015**, *51*, 9706–9709. [[CrossRef](#)]
46. Yu, W.; Xu, D.; Peng, T. Enhanced photocatalytic activity of g-C₃N₄ for selective CO₂ reduction to CH₃OH via facile coupling of ZnO: A direct Z-scheme mechanism. *J. Mater. Chem. A* **2015**, *3*, 19936–19947. [[CrossRef](#)]
47. Zhang, W. Studies on the Photo-Electrocatalytic Water Splitting Performance of BiVO₄-Cu₂O Photoelectrochemical Cell. Ph.D Thesis, Northwest University, Xi'an, China, 2021. [[CrossRef](#)]

Disclaimer/Publisher's Note: The statements, opinions and data contained in all publications are solely those of the individual author(s) and contributor(s) and not of MDPI and/or the editor(s). MDPI and/or the editor(s) disclaim responsibility for any injury to people or property resulting from any ideas, methods, instructions or products referred to in the content.